Materials Science and Engineering: A. Volume 799, 2 January 2021, Article number 140165
DOI: 10.1016/j.msea.2020.140165

Interaction between $Fe_{66}Cr_{10}Nb_5B_{19}$ metallic glass and aluminum during Spark Plasma Sintering

Dina V. Dudina[a,b,c] *, Boris B. Bokhonov[c], Igor S. Batraev[a], Yusif N. Amirastanov[b], Arina V. Ukhina[c], Ivanna D. Kuchumova[a,b], Mikhail A. Legan[a,b], Aleksey N. Novoselov[a], Konstantin B. Gerasimov[c], Ivan A. Bataev[b], Konstantinos Georgarakis[d], Guilherme Yuuki Koga[e], Yaofeng Guo[e], Walter José Botta[e], Alberto Moreira Jorge Jr.[e,f]

[a] Lavrentyev Institute of Hydrodynamics SB RAS, Lavrentyev Ave. 15, Novosibirsk, 630090, Russia

[b] Novosibirsk State Technical University, K. Marx Ave. 20, Novosibirsk, 630073, Russia

[c] Institute of Solid State Chemistry and Mechanochemistry SB RAS, Kutateladze str. 18, Novosibirsk, 630128, Russia

[d] School of Aerospace, Transport and Manufacturing, Cranfield University, Cranfield MK43 0AL, UK

[e] Department of Materials Science and Engineering, Federal University of São Carlos, Via Washington Luiz, km 235, São Carlos, SP 13565-905, Brazil

[f] Grenoble Alpes University, CNRS, LEPMI and SIMAP, F-38000 Grenoble, France

***Corresponding author**

Dina Dudina, Dr. Sci.
Institute of Solid State Chemistry and Mechanochemistry SB RAS
Kutateladze str. 18, Novosibirsk, 630128, Russia
E-mail: dina1807@gmail.com

Abstract
In the area of metal matrix composites, novel reinforcing options are currently being evaluated. Particles of amorphous alloys present an interesting possibility to reinforce soft metals. In the present work, the interaction between $Fe_{66}Cr_{10}Nb_5B_{19}$ metallic glass and aluminum during Spark Plasma Sintering (SPS) was studied for the first time. In order to trace the phase and microstructural changes upon sintering, mixtures containing 20 vol.% and 50 vol.% of metallic glass were subjected to SPS at 500–570 ºC. After SPS at 500 ºC, no reaction layer between the metallic glass particles and aluminum was observed. After SPS at 570 ºC, a reaction layer containing Fe_2Al_5 and $FeAl_3$ formed around the Fe-based cores. The Vickers hardness of composites obtained from mixtures containing 20 vol. % $Fe_{66}Cr_{10}Nb_5B_{19}$ at 540 ºC was 75 HV and increased to 280 HV after sintering at 570 ºC due to the formation of thicker reaction layers at the interface. The hardness of the composite sintered from the mixture containing 20 vol. % $Fe_{66}Cr_{10}Nb_5B_{19}$ at 570 ºC was between the values predicted by Reuss and Voigt models. Comparison of results of SPS of the powder mixtures with those of SPS of a pre-compacted pellet and electric current-free annealing suggests that local heating at the interface caused by interfacial resistance may be an important factor influencing the reaction advancement at the interface and the formation of Al-containing intermetallics.

Keywords: metal matrix composites, sintering, microstructure, scanning electron microscopy, hardness.

1. Introduction

Powder metallurgy offers higher microstructure versatility for metal matrix composites (MMCs) as compared with casting or infiltration methods [1]. The powder metallurgy approach allows obtaining microstructures that cannot be achieved by other processing methods. In recent years, significant effort has been directed to finding new types of reinforcements for MMCs and selecting suitable processing conditions of the composites to exploit the benefits of these reinforcements. New types of reinforcements include metallic glasses [2–5], high-entropy alloys [6–8] and quasicrystals [9–11] or their derivatives, which are phases forming upon the reaction of quasicrystals with the matrix [10, 12]. When the reinforcing alloy is to be preserved in the metastable state, the schedule of the heat treatment of the composites should be carefully selected. The very possibility of using metastable phases as reinforcements and retaining metastable structures and configurations in the composites exists owing to the availability of rapid sintering techniques, such as spark plasma sintering (SPS) [13].

Reinforcing aluminum and its alloys with metallic glass inclusions is among the modern trends in the development of aluminum matrix composites [14–25]. An approach to consolidation of metallic glass-reinforced MMCs based on the advantages given by the viscous flow of metallic glass in the supercooled liquid region was elaborated [3–5]: the consolidation temperature is to be selected within the supercooled liquid region. It is also possible to conduct consolidation below the glass transition temperature using high pressures to densify the matrix [17].

The interaction at the interface is a key phenomenon in the phase evolution, bonding between the phases, and mechanical properties of the composites. In metallic glass-reinforced metal matrix composites, the interaction between the matrix and the

glassy reinforcement is important for controlling both the phase stability and mechanical properties [22, 24]. Wang et al. [17] showed that, after sintering at a low temperature (300 ºC), the interfacial layer formed between Zr-based metallic glass and an Al-based matrix by interdiffusion was only a few nanometers thick. The layer provided good bonding between the metallic glass and the Al alloy matrix. By using SPS and hot extrusion conducted at a temperature below the crystallization temperature of the metallic glass, Guan et al. [24] preserved the cores of the reinforcing particles amorphous with only thin outer layers crystallized and reacted with aluminum to form $FeAl_3$. The formation of reaction layers was suggested as a positive structural feature from the viewpoint of load transfer from the soft and weak matrix to the hard shell and core.

In our previous work, we have shown that amorphous or partially amorphous materials can be produced from a $Fe_{66}Cr_{10}Nb_5B_{19}$ alloy by gas atomization and detonation spraying [26]. To our best knowledge, the influence of the SPS conditions on the interfacial interaction between the $Fe_{66}Cr_{10}Nb_5B_{19}$ metallic glass and aluminum has not been studied. In a SPS process, the material normally experiences the action of pressure and is heated by pulsed electric current. The mode of heating creates specific conditions for electrically conductive materials, which may include overheating at the inter-particle contacts or interfaces between different phases.

The goal of the present work was to trace the structural evolution during SPS of Al–$Fe_{66}Cr_{10}Nb_5B_{19}$ powder mixtures and to study its effect on the hardness of the composites. Al–$Fe_{66}Cr_{10}Nb_5B_{19}$ mixtures containing 20 vol. % and 50 vol. % of the glassy alloy were consolidated. Two concentrations of metallic glass in the mixture were used to produce an Al matrix composite reinforced with particles of metallic glass

or its derivatives and a composite, to which both starting components could contribute equally (volume-based). In the latter, the metallic glass acts as a reactant to form significant amounts of new phases when sintered at 570 ºC. High concentrations of the metallic glass particles in the aluminum matrix can be encountered in the case of particle agglomeration in certain areas. By deliberately preparing such compositions, we can "model" the outcomes of agglomeration in terms of the structural evolution and chemical reactions. The influence of the sintering temperature and cold pressing of the powder mixture before SPS on the phase compositions and microstructure of the composites was investigated. Conditions of SPS were selected such that 1) consolidation without the interfacial reactions could take place; 2) the interfacial reactions were allowed to proceed to yield significant amounts of the reaction products.

2. Materials and Methods

2.1. Starting materials

Gas-atomized powders of $Fe_{66}Cr_{10}Nb_5B_{19}$ and aluminum were used in the present study. The Al powder had a purity of 99.9% (PAD-6, average particle size 6 μm, "VALKOM-PM", Volgograd, Russia). For preparing the $Fe_{66}Cr_{10}Nb_5B_{19}$ master alloy, commercial-purity metals and alloys were used as starting materials: Fe-B alloy (B content 16.54 wt.%, ACL Metais, Araçariguama, Brazil), Fe-Nb alloy (Nb content 66.4 wt.%, ACL Metais, Araçariguama, Brazil), metallic chromium (Cr content >99.3 wt.%, ACL Metais, Araçariguama, Brazil), and metallic iron (Fe content >99.5 wt.%, Höganäs, Mogi das Cruzes, Brazil). The $Fe_{66}Cr_{10}Nb_5B_{19}$ alloy powder was obtained by argon gas atomization using a HERMIGA 75/5VI gas atomizer (Phoenix Scientific Industries Ltd., Hailsham, East Sussex, UK). The <45 μm fraction was separated by sieving. The Al–$Fe_{66}Cr_{10}Nb_5B_{19}$ powder mixtures were prepared using a horizontal low-

energy mixer with a plastic container and steel balls. The mixing time was 3 h. No shape changes of the particles occurred during mixing. Al–$Fe_{66}Cr_{10}Nb_5B_{19}$ mixtures containing 20 vol. % and 50 vol. % of the glassy alloy were prepared.

2.2. Consolidation of the powders

Sintering of the powders was carried out using a SPS Labox 1575 apparatus (SINTER LAND Inc., Japan) in forevacuum at a uniaxial pressure of 40 MPa. The die/punch assembly consisted of a graphite die of 20 mm inner diameter and 50 mm outer diameter, and graphite punches. The die wall was lined with graphite foil 200 μm thick. The circles of the same foil were placed between the flat ends of the punches and the sample. Al–$Fe_{66}Cr_{10}Nb_5B_{19}$ mixtures were subjected to SPS at 500 ºC, 540 ºC, and 570 ºC. The heating rate was 50 ºC min^{-1}. The holding time at the maximum temperature was 3 min. The temperature during the sintering process was measured by a thermocouple inserted into a 5-mm deep hole in the wall of the graphite die. Sintering experiments were conducted on Al–$Fe_{66}Cr_{10}Nb_5B_{19}$ mixtures and the $Fe_{66}Cr_{10}Nb_5B_{19}$ alloy powder. Post-sintering annealing of the Al–20 vol.% $Fe_{66}Cr_{10}Nb_5B_{19}$ sample was conducted in forevacuum at 570 ºC for 30 min. A SPS experiment with a cold-pressed Al–20 vol.% $Fe_{66}Cr_{10}Nb_5B_{19}$ pellet was also conducted. For that, a 10-mm diameter pellet was obtained by compaction in a hydraulic press at 400 MPa at room temperature. The pellet was sintered by SPS at 540 ºC in a graphite die of 10 mm inner diameter and 50 mm outer diameter. A 10-mm sample of the same composition was also sintered from the powder mixture (without the pre-compaction stage) at the same temperature.

2.3. Characterization of the powders and sintered composites

The $Fe_{66}Cr_{10}Nb_5B_{19}$ alloy powder was investigated by differential scanning calorimetry (DSC) using a STA 449 F1 JUPITER thermal analysis instrument (Netzsch,

Selb, Germany). The analysis was conducted in a flow of argon at a heating rate of 10 ºC min^{-1}.

The density of the $Fe_{66}Cr_{10}Nb_5B_{19}$ alloy powder was measured using an argon pycnometer (Institute of Solid State Chemistry and Mechanochemistry SB RAS, Novosibirsk, Russia). A value of 7.58 g cm^{-3} was obtained. The theoretical densities of the composites were calculated using the rule of mixtures (applicable to composites, in which no reaction product formed at the interface).

The metallographic samples of the composites were prepared using standard polishing operations. The microstructure of the sintered samples was studied by scanning electron microscopy (SEM) using a TM-1000 Tabletop microscope (Hitachi, Japan) and a Hitachi S-3400N (Japan) microscope. Back-scattered electron images of the composites are reported. Energy-dispersive spectroscopy (EDS) was conducted using a NORAN Spectral System 7 (Thermo Fisher Scientific Inc., USA). The X-ray diffraction (XRD) patterns of the samples were recorded by a D8 ADVANCE diffractometer (Bruker AXS, Germany) with Cu Kα radiation.

The relative densities of the sintered composites were determined from precisely measured mass and dimensions of the samples. The porosity of the sample sintered at 570 ºC was determined by analyzing its cross-sectional images in ImageJ software (https://imagej.nih.gov). The volume content of the phases in the composite sintered at 570 ºC from the Al–20 vol.% $Fe_{66}Cr_{10}Nb_5B_{19}$ mixture was also determined using ImageJ. For that, 15 images recoded with ×500 magnification were analyzed.

2.4. Microhardness/hardness measurements

Vickers microhardness/hardness of the individual phases/composites was measured on the polished cross-sections using a DuraScan 50 hardness tester (EMCO-

TEST, Austria). The microhardness of different phases of the composites (Al matrix, reaction layers, Fe-based alloy cores) was measured at a load of 0.01 kg, while the hardness of the composite structures was measured at a load of 0.3 kg or 1 kg. The microhardness measurement load was selected considering the size of the particles/areas to be indented. When measuring the hardness of the composites, the indents were made to cover the multiphase structure of the material. The average values were determined from 10 measurements. Standard deviations are reported along with the average values.

3. Results

3.1. Characteristics of the $Fe_{66}Cr_{10}Nb_5B_{19}$ alloy powder and its SPS behavior

Figure 1 shows the XRD pattern of the $Fe_{66}Cr_{10}Nb_5B_{19}$ alloy powder. The main phase of the alloy is an amorphous phase, which is indicated by the presence of a halo on the XRD scan. Body-centered iron is present as a minor phase in the alloy. The DSC analysis of the powder showed that the glass transition temperature T_g and crystallization temperature T_x of the glassy phase is 521 ºC and 573 ºC, respectively.

The temperature in the center of a Fe-based alloy sample processed by SPS is about 50 degrees higher than the temperature of the wall of the graphite die, as calculated by Paul et al. [27] for a graphite die of 20 mm inner diameter and 50 mm outer diameter. Therefore, in our work, consolidation of composites at 500 ºC as measured by the thermocouple inserted in a hole in the die wall can be considered as occurring within the supercooled liquid region of the glass. The other two sintering temperatures, 540 ºC and 570 ºC, were selected to study the phase and structure changes caused by partial crystallization of the glass and chemical interaction of the Fe-based alloy with aluminum. It should be noted that, in the presence of aluminum, it is rather difficult to trace the evolution of the phase composition of the Fe-based alloy by the

XRD in composites with low initial concentrations of the alloy. For rationalizing the results of SPS of composites, it is helpful to obtain information on the structural changes occurring in the alloy upon treatment in the SPS in the absence of aluminum. For this purpose, we sintered the alloy powder at 500 ºC, 540 ºC and 570 ºC. By SPS at 500 ºC, it was practically impossible to produce a robust sample, as the sintered compacts tended to shatter after they were removed from the die. The XRD analysis of these compacts did not reveal any changes relative to the powder state of the alloy. SEM observations showed that the particles changed their shape to an extent, and the contacts between particles flattened. After SPS at 540 ºC and 570 ºC, the $Fe_{66}Cr_{10}Nb_5B_{19}$ samples were well consolidated and did not shatter upon the removal from the die. The XRD patterns of these samples show the beginning of crystallization, as the halo corresponding to the amorphous phase narrows (Fig. 2). Therefore, during sintering of composites containing the $Fe_{66}Cr_{10}Nb_5B_{19}$ alloy powder under the same sintering cycle, one can expect partial crystallization of metallic glass, in addition to the chemical reactions of the alloy components with aluminum.

The fracture surface of the sintered alloy samples showed that particles making the compact are no longer spherical (Fig. 3). Owing to the viscous flow of the alloy in the supercooled liquid region reached during the sintering cycle, the particles changed their shape significantly under the action of uniaxial pressure to fill the inter-particle pores.

3.2. Phase composition and microstructure of composites obtained by SPS of Al–20 vol.% $Fe_{66}Cr_{10}Nb_5B_{19}$ and Al–50 vol.% $Fe_{66}Cr_{10}Nb_5B_{19}$ powder mixtures

Figures 4 and 5 show the XRD patterns of composites obtained from the Al–20 vol.% $Fe_{66}Cr_{10}Nb_5B_{19}$ and Al–50 vol.% $Fe_{66}Cr_{10}Nb_5B_{19}$ powder mixtures, respectively.

The XRD pattern of the Al–20 vol.% $Fe_{66}Cr_{10}Nb_5B_{19}$ composite sintered at 500 ºC demonstrates reflections of face-centered cubic Al only (Fig. 4). In the XRD pattern of the composite containing 50 vol.% of the glassy alloy, a halo is visible confirming the presence of an amorphous phase in the sintered material after SPS at 500 ºC (Fig. 5).

After annealing at 570 ºC, the Al–20 vol.% $Fe_{66}Cr_{10}Nb_5B_{19}$ composite sintered at 500 ºC contained a product of the interfacial interaction, $FeAl_3$ (Fig. 4). The same reaction product was observed in the samples sintered at 540 ºC (both obtained from the powder mixture and pre-compacted pellet). The flat ends of the cold-pressed pellet differed in the metallic glass/aluminum ratio, as some aluminum squeezed to the surface of the composite pellet on one side after pressing. The XRD pattern shown in Fig. 4 was taken from the smoother side of the pellet, which was enriched with the Fe-based alloy, as confirmed by SEM observations. For this reason, reflections caused by the products of the interfacial reaction are visible on the pattern. However, it was difficult to distinguish the reaction layer on the corresponding SEM image, as shown below. The XRD pattern taken from the other side (flat end) showed only Al peaks. Taking the XRD pattern from the glassy alloy-enriched side was ultimately beneficial for the purpose of this study, as it allowed confirming that, at this temperature, the reinforcement alloy did react with aluminum, but the reaction layer was very thin – much thinner than in composites obtained by sintering at 570 ºC.

After SPS of the Al–20 vol.% $Fe_{66}Cr_{10}Nb_5B_{19}$ powder mixture at 570 ºC, the composite contains $FeAl_3$ and Fe_2Al_5 along with residual aluminum (Fig. 4). After SPS of Al–50 vol.% $Fe_{66}Cr_{10}Nb_5B_{19}$ at 570 ºC, no free aluminum was detected by the XRD (Fig. 5) indicating that it was fully consumed in the chemical reaction with the Fe-based alloy.

Figure 6 demonstrates the cross-sectional images of the composites obtained by SPS of Al–$Fe_{66}Cr_{10}Nb_5B_{19}$ powder mixtures. The images of composites sintered at 500 ºC (Fig. 6 a, b) show lamellae sticking to the surface of the alloy particles. The formation of such lamellae is a known effect in the practice of gas atomization and is explained by frequent particle/droplet collisions during the atomization process [28]. These lamellae are not seen in the microstructure of composites sintered at higher temperatures (Fig. 6 c, d, e), as they are consumed in the chemical reaction between the alloy and the matrix. Figure 7 shows the fracture surface of the Al–20 vol.% $Fe_{66}Cr_{10}Nb_5B_{19}$ composite sintered at 500 ºC. It can be seen that particles of the aluminum powder adhered to the particles of the glassy alloy. However, only a small fraction of the metallic glass particle surface is covered. The boundaries between the aluminum particles are clearly seen, which indicates poor consolidation of aluminum not accompanied by diffusion.

As the sintering temperature increases, the interfacial layer in composites obtained from Al–20 vol.% $Fe_{66}Cr_{10}Nb_5B_{19}$ appears and becomes thicker, as seen in Fig. 6 (a, c, d). After SPS at 570 ºC, layers 10–15 μm thick formed around the Fe-based alloy cores in the composite obtained from the Al–20 vol.% $Fe_{66}Cr_{10}Nb_5B_{19}$ powder mixture (Fig. 6 d). Upon the reaction between aluminum and iron, pores form in locations of aluminum particles, if aluminum is confined in a certain volume, owing to Kirkendall effect [29–31]. As aluminum plays a role of the matrix surrounding particles of the metallic glass in Al–20 vol.% $Fe_{66}Cr_{10}Nb_5B_{19}$ composites, we do not observe porosity related to Kirkendall effect. In the composite sintered from the Al–50vol.% $Fe_{66}Cr_{10}Nb_5B_{19}$ mixture, aluminum was fully consumed such that the reaction layers could not grow further and touched each other in the microstructure (Fig. 6 e).

Fe and Al elemental maps of a selected region of the cross-section of the composite consolidated by SPS of the Al–20 vol.% $Fe_{66}Cr_{10}Nb_5B_{19}$ powder mixture at 570 ºC are presented in Fig. 8. The maps confirm the absence of aluminum in the cores of the reinforcing particles and the presence of both iron and aluminum in the reaction layers. Additional information on the distribution of elements was obtained in the form of the point EDS analysis (Fig. 9). The spectra were taken from the characteristic areas of the composite's microstructure. It should be noted that, as boron is a light element, it was quite difficult to obtain reliable information on its concentration in different areas. Therefore, the structure of boron-containing phases in these composites remains an open question requiring further investigation. In the framework of the present article, we discuss the Al/Fe ratio in the reaction layer (Fig. 9); this ratio is close to that in the $FeAl_3$ phase. The matrix was mainly residual (unreacted) aluminum.

The composite obtained by SPS of the Al–50 vol.% $Fe_{66}Cr_{10}Nb_5B_{19}$ mixture at 570 ºC consists of spherical particles having a core-shell structure, as confirmed by SEM (Fig. 6 e) and elemental maps (Fig. 10). The pores between the core-shell particles were not eliminated, as the sintering temperature was too low to activate densification of the Fe-Al intermetallics.

Figure 11 shows the cross-section of the composite processed by SPS (at 500 ºC) followed by annealing (at 570 ºC). The microstructure of the annealed material agrees with results of the XRD and confirms the formation of a reaction layer about 7 μm thick. Figure 12 a, b allows comparing the thicknesses of the reaction layers forming at the interfaces in the composite obtained by SPS of the Al–20 vol.% $Fe_{66}Cr_{10}Nb_5B_{19}$ mixture at 570 ºC and the composite pre-sintered at 500 ºC and annealed at 570 ºC. During annealing, no electric current was passing through the sample. It can be seen that

the reaction layer is thinner in the sample subjected to annealing despite a longer duration of the process (30 min of annealing versus 3 min of SPS). The advancement of the reaction of the alloy with aluminum can be rationalized by assuming a possibility of local overheating at the inter-particle contacts and interfaces during SPS. Structural evidence suggesting the formation of high-temperature regions has been reported for other systems processed by SPS [7, 8, 32]. In the reaction layer formed in the composite obtained by SPS at 570 ºC, two phases differing in contrast can be distinguished (Fig. 12 a), which agrees with the XRD results. Bright branch-like areas contain a higher concentration of a larger atomic number element and thus should correspond to the Fe_2Al_5 phase, the gray background being $FeAl_3$. The phase enriched in Fe is observed near the Fe-based alloy cores. Previously, the separation of the reaction products into layers was observed by Yu et al. [33, 34]. The formation of layers with compositions close to $NbAl_3$ and $NiAl_3$ was observed when an Al–30 wt.% amorphous $Ni_{60}Nb_{40}$ alloy composite was annealed at 640 ºC. During the interfacial reaction, nickel diffused from the $Ni_{60}Nb_{40}$ particles to react with aluminum and form $NiAl_3$. At the same time, aluminum diffused into the reinforcement particles to react with the remaining niobium to form $NbAl_3$. Nickel was, therefore, mainly distributed in the outer layer, while niobium was mainly present in the core. It was found that, upon heating, the interaction between the alloy and aluminum was not detected before the alloy started crystallizing [33], which agrees with results obtained in the present work.

3.3. SPS processing of a cold-pressed Al–20 vol.% $Fe_{66}Cr_{10}Nb_5B_{19}$ pellet

Interestingly, in the cross-section of the composite obtained by SPS of the cold-pressed Al–20 vol.% $Fe_{66}Cr_{10}Nb_5B_{19}$ pellet, we do not see a reaction layer between the metallic glass and aluminum (Fig. 13). Some interaction was evidenced by the XRD

analysis, as discussed above (Fig. 4). The formation of a very thin reaction layer or the absence of one on some particles can be explained by lower local temperatures (in the interfacial regions) in this sample during SPS as compared with the sample sintered directly from the powder mixture at the same measured temperature (Fig. 6 c). In the SPS processing, some structural features of materials can depend on the sample size [13]. It should be noted that Fig, 6 c shows the microstructure of the compact of 20 mm diameter. We have confirmed that samples with diameters of 10 and 20 mm obtained by SPS of Al–20 vol.% $Fe_{66}Cr_{10}Nb_5B_{19}$ powder mixture at 540 ºC possess the same microstructure and phase composition. Therefore, the comparison made above is valid, as compacts of the same diameter can be compared.

The relative density of the cold-pressed Al–20 vol.% $Fe_{66}Cr_{10}Nb_5B_{19}$ pellet was 81%, which indicates plastic yielding of aluminum during pressing under a high applied pressure (400 MPa). Under these conditions, the oxide films present on the aluminum particles could break enabling metal-to-metal contact between the reinforcing alloy and the matrix in the pre-compacted material. Such a contact will possess a lower resistance than the contact, the formation of which is complicated by the presence of oxide films. So, after cold pressing, the contact conditions between the phases in the composite were better in terms of the contact resistance. A lower resistance could have resulted in the absence of overheating at the interface, in contrast to the sample processed without the pre-compaction stage.

3.4. Hardness of the sintered composites

The relative density of Al–20 vol.% $Fe_{66}Cr_{10}Nb_5B_{19}$ and Al–50 vol.% $Fe_{66}Cr_{10}Nb_5B_{19}$ composites consolidated by SPS at 500 ºC was measured to be 95% and 86%, respectively. The relative densities (porosities) of composites sintered at 540 ºC

and 570 ºC as well as their hardness and microhardness of the individual phases (characteristic regions) are given in Tables 1–2. The hardness of composites sintered at 500 ºC is not reported, as, during indentation, the metallic glass particles detached from the matrix.

4. Discussion

4.1. Analysis of the hardness values in relation to Voigt and Reuss models

Kim [35] analyzed the hardness variation with the volume fraction of hard particles in the particle-reinforced composites using models for the rule of mixtures and the finite element method. The results of the elastoplastic finite element analysis fitted better the iso-strain curve (Voigt model) at high volume fractions of hard particles and were close to the iso-stress curve (Reuss model) at low volume fractions of hard particles. Therefore, in composites containing a low concentration of hard particles in a soft aluminum matrix, the rule of mixtures should be valid in the form of Reuss model. For composites containing relatively high contents of the hard phase, Voigt model can be used to predict the hardness. The hardness value can also lie between these limits. As seen from Table 1, in composites having only thin layers of the reaction products (SPS at 540 ºC), the hardness was indeed close to the value predicted by Reuss model. The Vickers hardness of the composite sintered from the Al–20 vol.% $Fe_{66}Cr_{10}Nb_5B_{19}$ mixture at 570 ºC was found to be 280 HV (Table 2). A higher hardness of this composite as compared with that of the material sintered at 540 ºC is due to the formation of thick reaction layers at the interface. In the composite sintered at 570 ºC, the volume fraction of the Fe-based alloy (particle cores), reaction products and residual aluminum was 8%, 55% and 37%, respectively. The hardness of this composite was found to be between the values predicted by Reuss and Voigt models, as can be seen in

Table 2. It should be noted here that, due to limitations of the size of the particles and areas occupied by the individual phases in the cross-section of the sintered composites, the local hardness (microhardness) was measured using a lower load than that used for measuring the hardness of the composite. As higher hardness values are usually obtained at lower loads, the hardness values calculated from the microhardness of the individual phases using Reuss and Voigt models are somewhat overestimated. Full consumption of aluminum in the composite obtained from Al–50 vol.% $Fe_{66}Cr_{10}Nb_5B_{19}$ mixture at 570 ºC and the structure shown in Fig. 6 e do not lead to the efficient use of the available strengthening tools, as the hardness of the composite is lower than that predicted by the rule of mixtures (lower than the hardness of the softer component, Table 2).

Our results are in good agreement with those obtained for other systems. Liu et al. [8] showed that, in composites sintered from an Al–5 vol.% AlCoCrFeNi high-entropy alloy mixture, the thickness of the interfacial layer increases with the sintering temperature. The hardness determined by nano-indentation for the high-entropy alloy reinforcement, transition layer and matrix was 8.884 GPa, 2.376 GPa, and 0.470 GPa, respectively. When the SPS temperature was 560 ºC, a reaction layer with a thickness of 5–7 μm formed between the matrix and the reinforcing alloy. The yield strength of this composite was 105 MPa, which is somewhat higher than the value predicted by the Reuss model (86 MPa).

4.2. Features of the SPS process of metallic glass-aluminum composites

As a further development of this work, a more detailed characterization of the reaction products forming between the metallic glass and aluminum will be needed. The fine structure of the reaction layers and parameters of the crystalline structure of the

newly formed phases could help understand the complex diffusion processes in the multi-component system. Embedding gas-atomized powders of alloys in metallic matrices under conditions such that interfacial reactions are allowed to proceed to a certain degree appears to be a viable method of obtaining composites with core-shell particle reinforcements. Such composites are currently of interest [8, 24]. The use of SPS as a consolidation method is technologically attractive as, under properly selected sintering conditions, it offers a single-step fabrication of MMCs with partially amorphous core-intermetallic shell reinforcements. The formation of local regions, in which the temperature is higher than that of the particle volume, can be used to advantage for a quick synthesis of reaction layers modifying the composite's properties. The controlled growth of the reaction layer between aluminum and $Fe_{66}Cr_{10}Nb_5B_{19}$ is, therefore, an efficient approach to tailoring the hardness of the composites. Here, SPS as a consolidation method of aluminum–metallic glass mixtures offers a possibility of fast one-step fabrication of composites with partially amorphous core-crystalline shell reinforcements.

5. Conclusions

This work has allowed us to draw the following conclusions:

1. During SPS at 500 ºC, no interfacial reaction product formed between the $Fe_{66}Cr_{10}Nb_5B_{19}$ metallic glass particles and aluminum. At 570 ºC, the reaction advancement resulted in the formation of layers 10–15 μm thick containing Fe_2Al_5 and $FeAl_3$ (around the Fe-based cores) in the composite sintered from the Al–20 vol.% $Fe_{66}Cr_{10}Nb_5B_{19}$ mixture.
2. The hardness of the composites depends on the sintering temperature and composition of the starting Al–$Fe_{66}Cr_{10}Nb_5B_{19}$ powder mixture. The composite

sintered at 570 ºC from the mixture containing 20 vol.% $Fe_{66}Cr_{10}Nb_5B_{19}$ showed a hardness of 280 HV due to the formation of the reaction layers. This value is between those predicted by Reuss and Voigt models. In composites with thin layers of the reaction products (SPS at 540 ºC), the hardness was much lower and close to the value predicted by Reuss model.

3. Experiments with a pre-compacted composite and annealing of the sintered composites in the absence of electric current showed that local heating at the interface (interfacial resistance) should be considered an important factor in the phase formation at the interface between the metallic glass and aluminum.

Acknowledgements

This work was supported by the Ministry of Science and Higher Education of the Russian Federation.

The Brazilian authors acknowledge the financial support of FAPESP (thematic project, Grant Number 2013/05987-8).

The authors are grateful to Vyacheslav V. Markushin for his help in the preparation of metallographic samples.

Conflict of interest

The authors declare no conflict of interest.

Data Availability Statement

The raw/processed data required to reproduce these findings are included in the Materials and Methods section.

References

1. J. M. Torralba, C. E. da Costa, F. Velasco, P/M aluminum matrix composites: an overview, J. Mater. Proc. Tech. 133 (2003) 203–206. https://doi.org/10.1016/S0924-0136(02)00234-0.
2. S. Scudino, K. B. Surreddi, S. Sager, M. Sakaliyska, J. S. Kim, W. Löser, J. Eckert, Production and mechanical properties of metallic glass-reinforced Al-based metal matrix composites, J. Mater. Sci. 43 (2008) 4518–4526. https://doi.org/10.1007/s10853-008-2647-5.
3. D. V. Dudina, K. Georgarakis, Y. Li, M. Aljerf, A. LeMoulec, A. R. Yavari, A. Inoue, A magnesium alloy matrix composite reinforced with metallic glass, Comp. Sci. Technol. 69 (2009) 2734–2736. https://doi.org/10.1016/j.compscitech.2009.08.001.
4. D. V. Dudina, K. Georgarakis, Y. Li, M. Aljerf, M. Braccini, A. R. Yavari, A. Inoue, Cu-based metallic glass particle additions to significantly improve overall compressive properties of an Al alloy, Composites Part A 41 (2010) 1551–1557. https://doi.org/10.1016/j.compositesa.2010.07.004.
5. M. Aljerf, K. Georgarakis, D. Louzguine-Luzgin, A. Le Moulec, A. Inoue, A. R. Yavari, Strong and light metal matrix composites with metallic glass particulate reinforcement, Mater. Sci. Eng. A 532 (2012) 325–330. https://doi.org/10.1016/j.msea.2011.10.098.
6. Z. Yuan, W. Tian, F. Li, Q. Fu, X. Wang, W. Qian, W. An, 2020. Effect of heat treatment on the interface of high-entropy alloy particles reinforced aluminum matrix composites. J. Alloys Compd. 822. 153658.39. https://doi.org/10.1016/j.jallcom.2020.153658.

7. Z. Yuan, W. Tian, F. Li, Q. Fu, Y. Hu, X. Wang, Microstructure and properties of high-entropy alloy reinforced aluminum matrix composites by spark plasma sintering. J. Alloys Compd. 806 (2019) 901–908. https://doi.org/10.1016/j.jallcom.2019.07.185.
8. Y. Liu, J. Chen, Z. Li, X. Wang, X. Fan, J. Liu, Formation of transition layer and its effect on mechanical properties of AlCoCrFeNi high-entropy alloy/Al composites. J. Alloys Compd. 780 (2019) 558–564. https://doi.org/10.1016/j.jallcom.2018.11.364
9. F. Ali, S. Scudino, G. Liu, V.C. Srivastava, N.K. Mukhopadhyay, M. Samadi Khoshkhoo, K. G. Prashanth, V. Uhlenwinkel, M. Calin, J. Eckert, Modeling the strengthening effect of Al–Cu–Fe quasicrystalline particles in Al-based metal matrix composites, J. Alloys Compd. 536 (2012) S130– S133. https://doi.org/10.1016/j.jallcom.2011.12.022.
10. F. Ali, S. Scudino, M.S. Anwar, R.N. Shahid, V.C. Srivastava, V. Uhlenwinkel, M. Stoica, G. Vaughan, J. Eckert. Al-based metal matrix composites reinforced with Al–Cu–Fe quasicrystalline particles: Strengthening by interfacial reaction, J. Alloys Compd. 607 (2014) 274–279. https://doi.org/10.1016/j.jallcom.2014.04.086.
11. L. Lityńska-Dobrzyńska, J. Dutkiewicz, K. Stan-Głowińska, W. Wajda, L. Dembinski, C. Langlade, C. Coddet, Characterization of aluminium matrix composites reinforced by Al–Cu–Fe quasicrystalline particles, J. Alloys Compd. 643 (2015) S114–S118. https://doi.org/10.1016/j.jallcom.2014.11.125.
12. A. Joseph, V. Gauthier-Brunet, A. Joulain, J, Bonneville, S. Dubois, J.-P. Monchoux, F. Pailloux, Mechanical properties of Al/ω-Al-Cu-Fe composites

synthesized by the SPS technique, Mater. Charact. 145 (2018) 644–652. https://doi.org/10.1016/j.matchar.2018.09.025

13. E. A. Olevsky, D. V. Dudina, Field-Assisted Sintering: Science and Applications, Springer International Publishing, Cham, Switzerland, 2018.
14. P. Yu, K. B. Kim, J. Das, F. Baier, W. Xu, J. Eckert, Fabrication and mechanical properties of Ni-Nb metallic glass particle-reinforced Al-based metal matrix composite, Scr. Mater. 54 (2006) 1445–1450. https://doi.org/10.1016/j.scriptamat.2006.01.001.
15. S. Scudino, G. Liu, K. G. Prashanth, B. Bartusch, K. B. Surreddi, B. S. Murty, J. Eckert, Mechanical properties of Al-based metal matrix composites reinforced with Zr-based glassy particles produced by powder metallurgy, Acta Mater. 57 (2009) 2029–2039. https://doi.org/10.1016/j.actamat.2009.01.010.
16. Z. Wang, S. Scudino, M. Stoica, W. W. Zhang, J. Eckert, Al-based matrix composites reinforced with short Fe-based metallic glassy fiber, J. Alloy Compd. 651 (2015) 170–175. https://doi.org/10.1016/j.jallcom.2015.08.098.
17. Z. Wang, K. Georgarakis, K. Nakayama, Y. Li, A. Tsarkov, G. Xie, D. Dudina, D. V, Louzguine-Luzgin, A. R. Yavari, 2016. Microstructure and mechanical behavior of metallic glass fiber-reinforced Al alloy matrix composites. Sci. Rep. 6, 24384. https://doi.org/10.1038/srep24384.
18. W. W. Zhang, Y. Hu, Z. Wang, C. Yang, G. Q. Zhang, K. G. Prashanth, C. Suryanarayana, A novel high-strength Al-based nanocomposite reinforced with Ti-based metallic glass nanoparticles produced by powder metallurgy, Mater. Sci. Eng. A 734 (2018) 34–41. https://doi.org/10.1016/j.msea.2018.07.082.

19. T. He, T. Lu, N. Ciftci, H. Tan, V. Uhlenwinkel, K. Nielsch, S. Scudino, Mechanical properties and tribological behavior of aluminum matrix composites reinforced with Fe-based metallic glass particles: Influence of particle size, Powder Technol. 361 (2020) 512–519. https://doi.org/10.1016/j.powtec.2019.11.088.
20. T. He, O. Ertuğrul, N. Ciftci, V. Uhlenwinkel, K. Nielsch, S. Scudino, Effect of particle size ratio on microstructure and mechanical properties of aluminum matrix composites reinforced with $Zr_{48}Cu_{36}Ag_8Al_8$ metallic glass particles, Mater. Sci. Eng. A 742 (2019) 517–525. https://doi.org/10.1016/j.msea.2018.11.007.
21. S. Jayalakshmi, S. Gupta, S. Sankaranarayanan, S. Sahu, M. Gupta, Structural and mechanical properties of $Ni_{60}Nb_{40}$ amorphous alloy particle reinforced Al-based composites produced by microwave-assisted rapid sintering, Mater. Sci. Eng. A 581 (2013) 119–127. https://doi.org/10.1016/j.msea.2013.05.072.
22. O. Ertugrul, T. He, R. N. Shahid, S. Scudino, 2019. Effect of heat treatment on microstructure and mechanical properties of Al 2024 matrix composites reinforced with $Ni_{60}Nb_{40}$ metallic glass particles. J. Alloys Compd. 808. 151732. https://doi.org/10.1016/j.jallcom.2019.151732.
23. M. S. Xie, C. Suryanarayana, Y. L. Zhao, W. W. Zhang, C. Yang, G. Q. Zhang, Y. N. Fu, Z. Wang, 2020. Abnormal hot deformation behavior in a metallic-glass-reinforced Al-7075 composite. Mater. Sci. Eng. A 139212. https://doi.org/10.1016/j.msea.2020.139212.
24. H. D. Guan, C. J. Li, P. Gao, K. G. Prashanth, J. Tan, J. Eckert, J. M. Tao, J. H. Yi, 2020. Aluminum matrix composites reinforced with metallic glass particles

with core-shell structure. Mater. Sci. Eng. A. 771. 138630. https://doi.org/10.1016/j.msea.2019.138630.

25. D. V. Dudina, K. Georgarakis, A. R. Yavari, Metal matrix composites reinforced with metallic glass particles: state of the art. In: Metal Matrix Composites, Ed. J. Paulo Davim, Nova Science Publishers, Inc., USA, 2012, pp.1–30.
26. I. D. Kuchumova, I. S. Batraev, V. Yu. Ulianitsky, A. A. Shtertser, K. B. Gerasimov, A. V. Ukhina, N. V. Bulina, I. A. Bataev, G. Y. Koga, Y. Guo, W. J. Botta, H. Kato, T. Wada, B. B. Bokhonov, D. V. Dudina, A. Moreira Jorge Jr., 2019. Formation of metallic glass coatings by detonation spraying of a $Fe_{66}Cr_{10}Nb_5B_{19}$ powder. Metals. 9. 846. https://doi.org/10.3390/met9080846.
27. T. Paul, A. Singh, S. P. Harimkar, 2017. Densification and crystallization in Fe–based bulk amorphous alloy spark plasma sintered in the supercooled liquid region. 19. 1700224. https://doi.org/10.1002/adem.201700224.
28. X. Li, Q. Zhu, S. Shu, J. Fan, Sh. Zhang, Fine spherical powder production during gas atomization of pressurized melts through melt nozzles with a small inner diameter, Powder Technol. 356 (2019) 759–768. https://doi.org/10.1016/j.powtec.2019.09.023.
29. D. V. Dudina, B. B. Bokhonov, A. K. Mukherjee, 2016. Formation of aluminum particles with shell morphology during pressureless Spark Plasma Sintering of Fe-Al mixtures: current-related or Kirkendall effect? Materials. 9. 375. https://doi.org/10.3390/ma9050375.
30. H. Gao, Y. He, P. Shen, J. Zou, N. Xu, Y. Jiang, B. Huang, C. T. Liu, Porous FeAl intermetallics fabricated by elemental powder reactive synthesis,

Intermetallics 17 (2009) 1041–1046. https://doi.org/10.1016/j.intermet.2009.05.007.

31. H. Y. Gao, Y. H. He, P. Z. Shen, Y. Jiang, C. T. Liu, Effect of pressure on pore structure of porous FeAl intermetallics, Adv. Powder Technol. 26 (2015) 882–886. https://doi.org/10.1016/j.apt.2015.03.002.
32. K. L. Firestein, A. E. Steinman, I. S. Golovin, J. Cifre, E. A. Obraztsova, A. T. Matveev, A. M. Kovalskii, O. I. Lebedev, D. V. Shtansky, D. Golberg, Fabrication, characterization, and mechanical properties of spark plasma sintered Al–BN nanoparticle composites, Mater. Sci. Eng. A 642 (2015) 104–112. https://doi.org/10.1016/j.msea.2015.06.059.
33. P. Yu, L. C. Zhang, W. Y. Zhang, J. Das, K. B. Kim, J. Eckert, Interfacial reaction during the fabrication of $Ni_{60}Nb_{40}$ metallic glass particles-reinforced Al based MMCs, Mater. Sci. Eng. A444 (2007) 206–213. https://doi.org/10.1016/j.msea.2006.08.077.
34. P. Yu, S. Venkataraman, J. Das, L. C. Zhang, W. Zhang, J. Eckert, Effect of high pressure during the fabrication on the thermal and mechanical properties of amorphous $Ni_{60}Nb_{40}$ particle-reinforced Al-based metal matrix composites, J. Mater. Res. 22 (2007) 1168–1173. https://doi.org/10.1557/JMR.2007.0158.
35. H. S. Kim, On the rule of mixtures for the hardness of particle reinforced composites, Mater. Sci. Eng. A 289 (2000) 30–33. https://doi.org/10.1016/S0921-5093(00)00909-6.

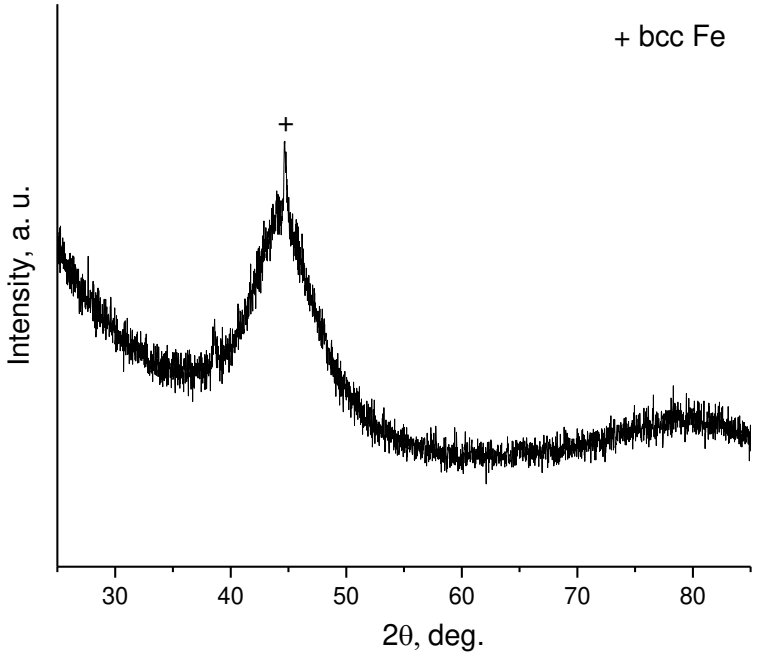

Figure 1. XRD pattern of the $Fe_{66}Cr_{10}Nb_5B_{19}$ gas-atomized powder, fraction <45 μm.

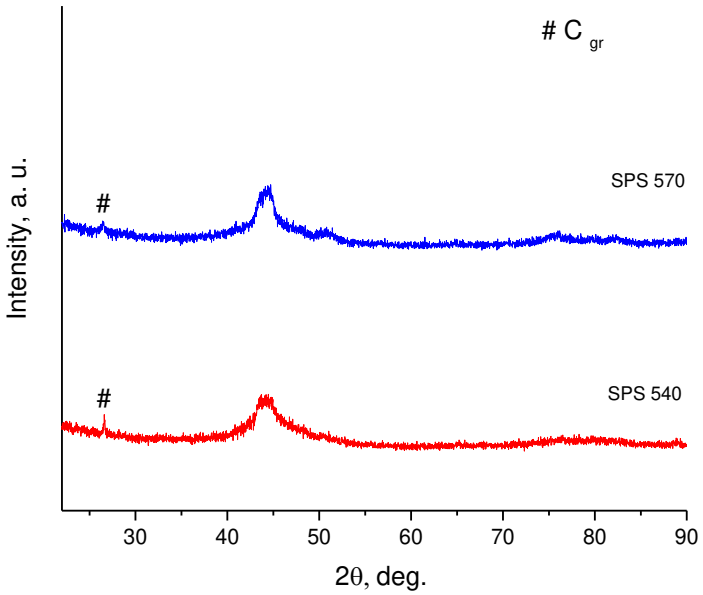

Figure 2. XRD patterns of samples obtained by SPS of the $Fe_{66}Cr_{10}Nb_5B_{19}$ alloy powder at 540 ºC and 570 ºC.

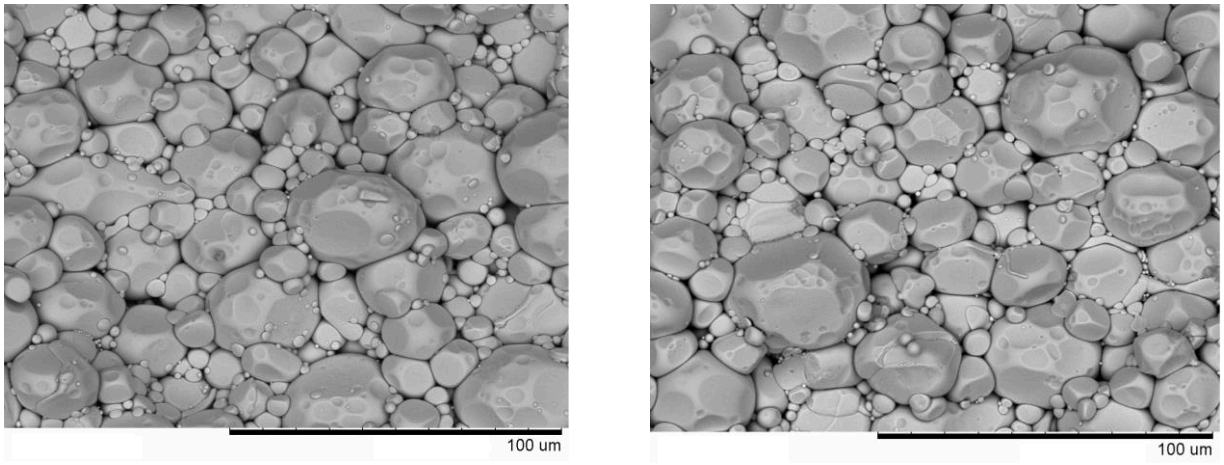

a **b**

Figure 3. Fracture surface of samples obtained by SPS of the $Fe_{66}Cr_{10}Nb_5B_{19}$ alloy powder at (a) 540 ºC and (b) 570 ºC.

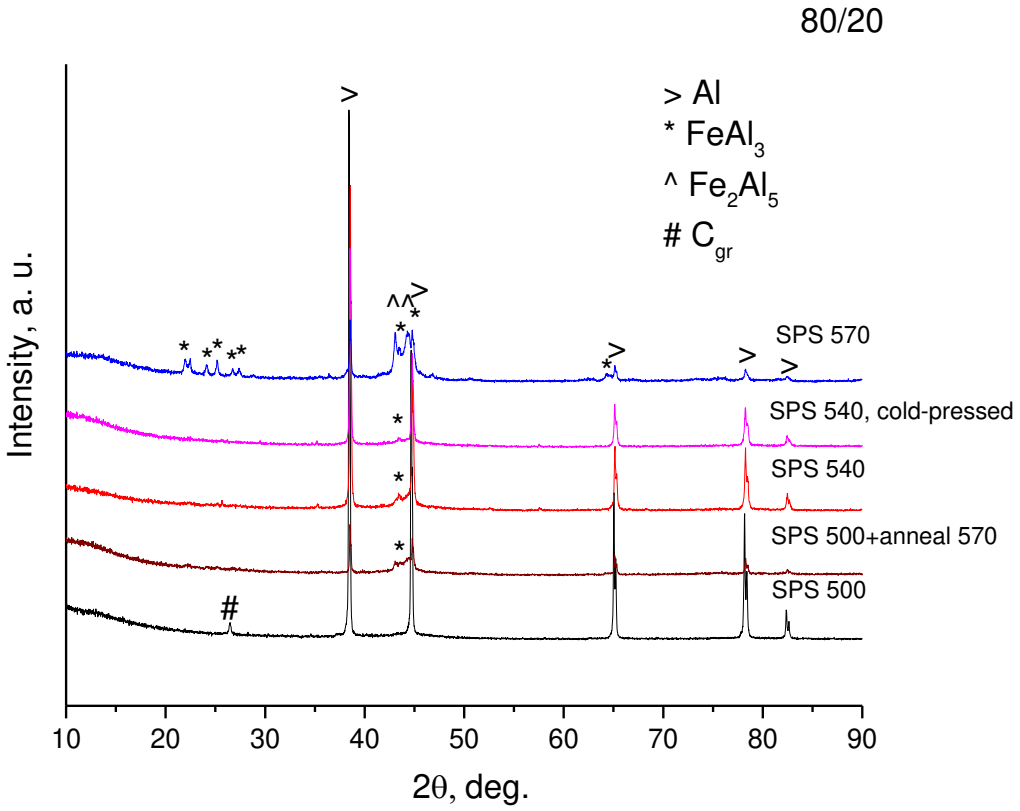

Figure 4. XRD patterns of composites obtained from the Al–20 vol.% $Fe_{66}Cr_{10}Nb_5B_{19}$ powder mixture: SPS at 500 ºC; SPS at 500 ºC followed by annealing at 570 ºC for 30 min; SPS at 540 ºC; SPS of the cold-pressed pellet at 540 ºC and SPS at 570 ºC. The graphite reflection in the pattern of the sample sintered at 500 ºC is due to small pieces of graphite foil adhered to the sample's surface after SPS.

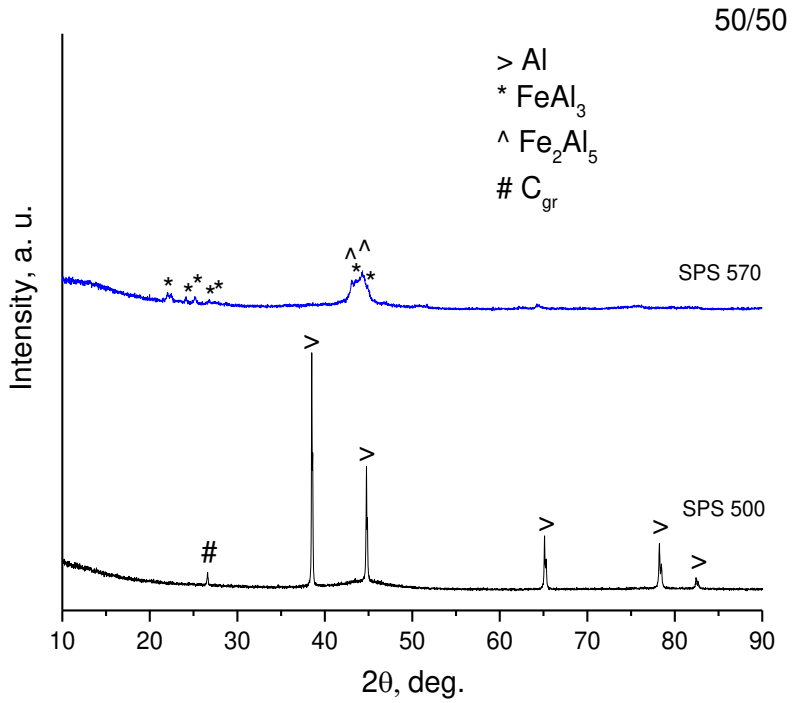

Figure 5. XRD patterns of composites obtained by SPS of the Al–50 vol.% $Fe_{66}Cr_{10}Nb_5B_{19}$ powder mixture at 500 ºC and 570 ºC.

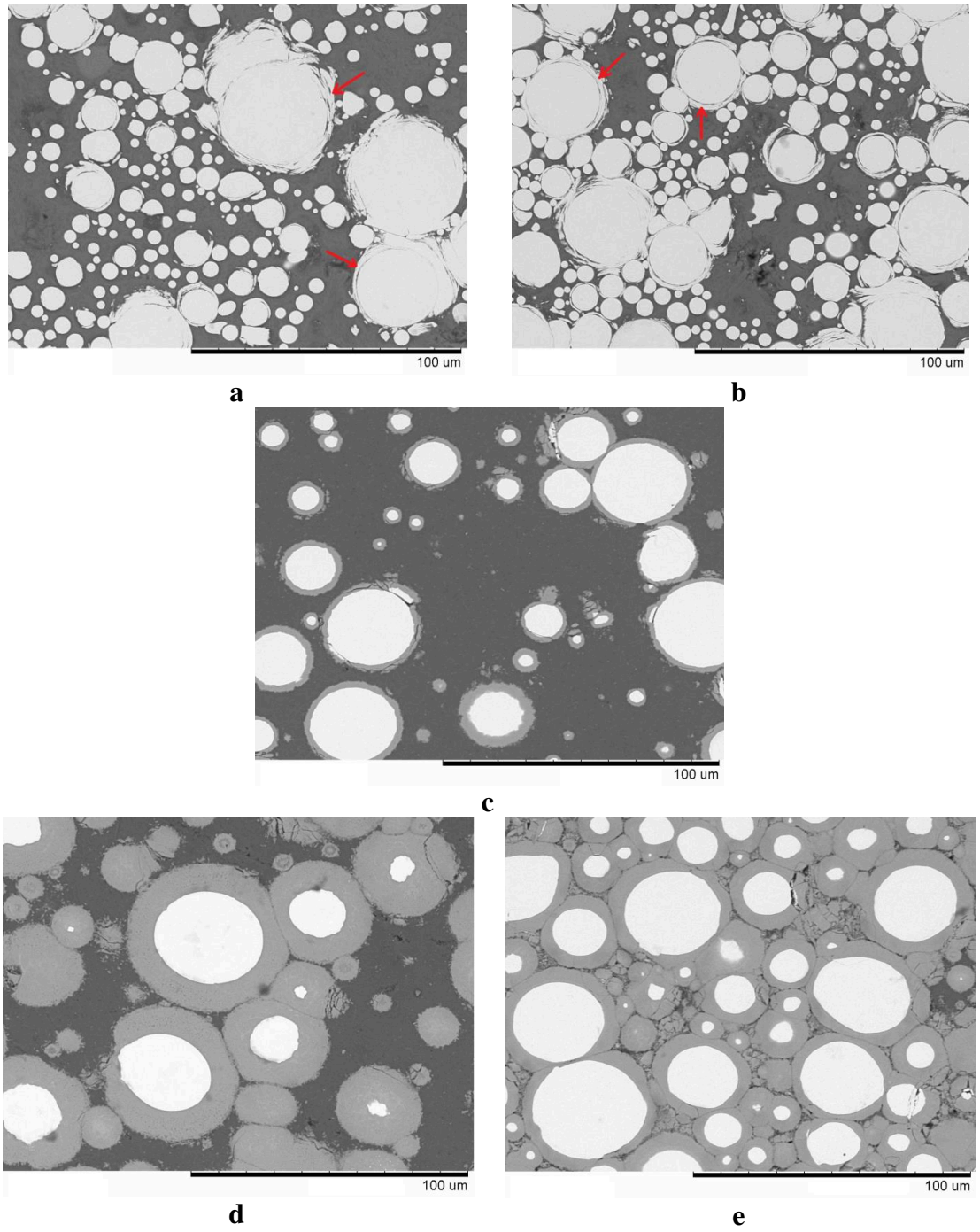

Figure 6. Cross-sections of composites obtained by SPS from Al–$Fe_{66}Cr_{10}Nb_5B_{19}$ powder mixtures containing 20 vol.% and 50 vol.% $Fe_{66}Cr_{10}Nb_5B_{19}$: (a) 500 ºC, 80/20; (b) 500 ºC, 50/50; (c) 540 ºC, 80/20; (d) 570 ºC, 80/20; (e) 570 ºC, 50/50. The lamellae on the surface of the particles are marked by red arrows in (a, b).

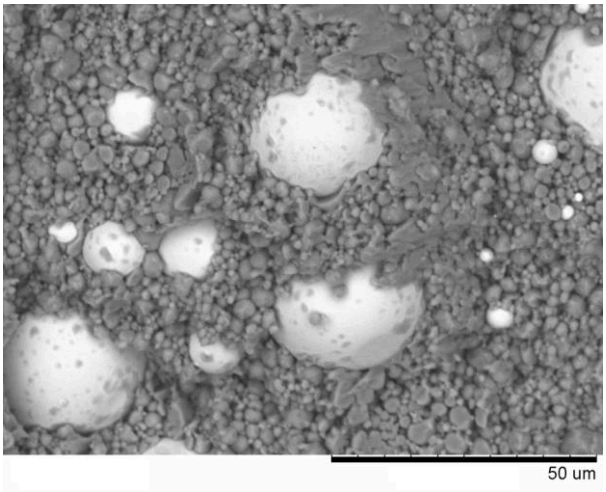

Figure 7. Fracture surface of the composite obtained by SPS of the Al–20 vol.% $Fe_{66}Cr_{10}Nb_5B_{19}$ powder mixture at 500 ºC.

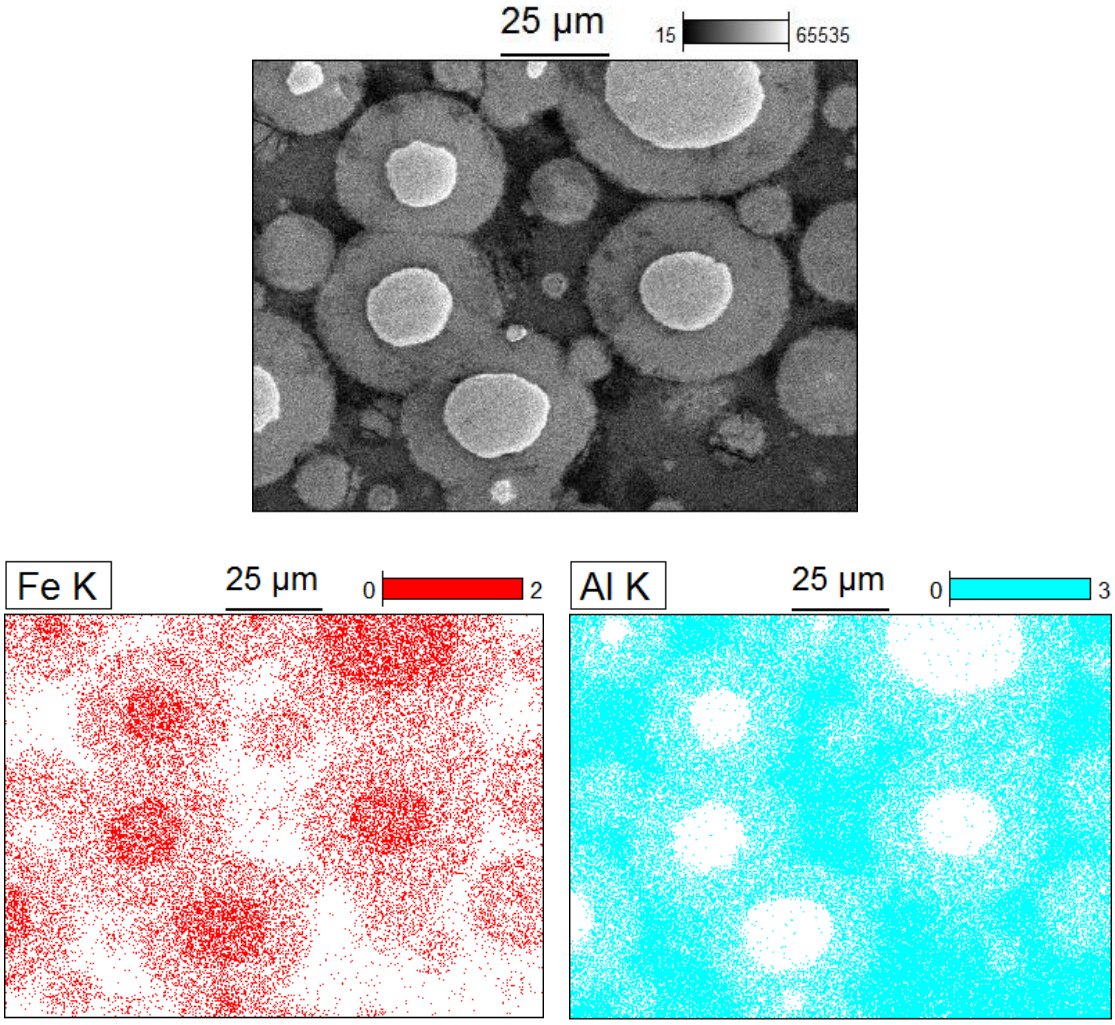

Figure 8. Fe and Al maps from a selected area of the cross-section of the composite obtained by SPS of the Al–20 vol.% $Fe_{66}Cr_{10}Nb_5B_{19}$ powder mixture at 570 ºC.

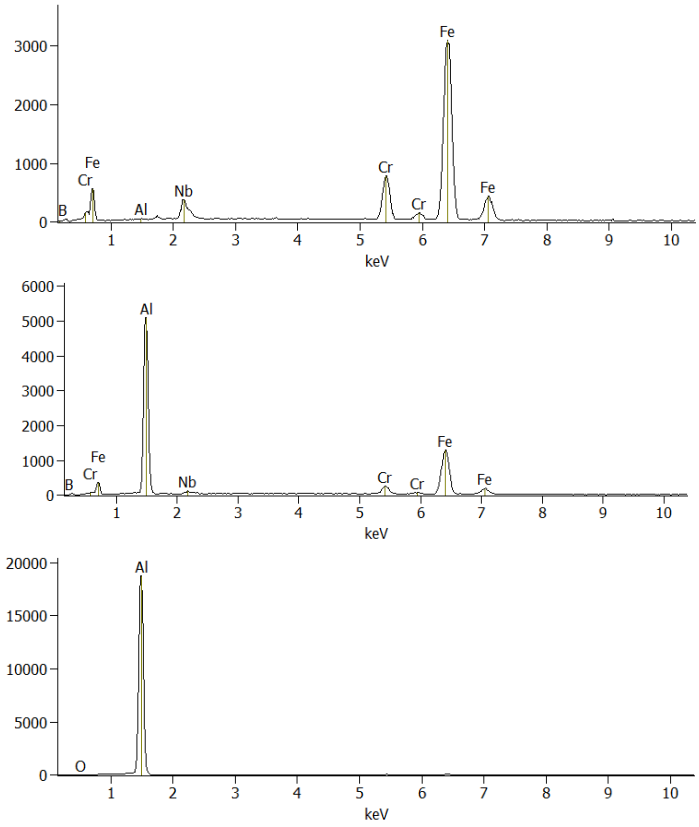

Fe-based core, at.%
B 4.75±1.38
Al 1.51±0.18
Cr 12.55±0.21
Fe 78.80±0.57
Nb 2.40±0.84

Reaction layer, at.%
Al 75.62±0.43
Cr 2.84±0.11
Fe 20.65± 0.24
Nb 0.89± 0.42

Al matrix, at.%
O 2.52± 0.36
Al 97.48±0.41

Figure 9. EDS spectra from points in the characteristic areas of the microstructure of the composite obtained by SPS of the Al–20 vol.% $Fe_{66}Cr_{10}Nb_5B_{19}$ powder mixture at 570 ºC.

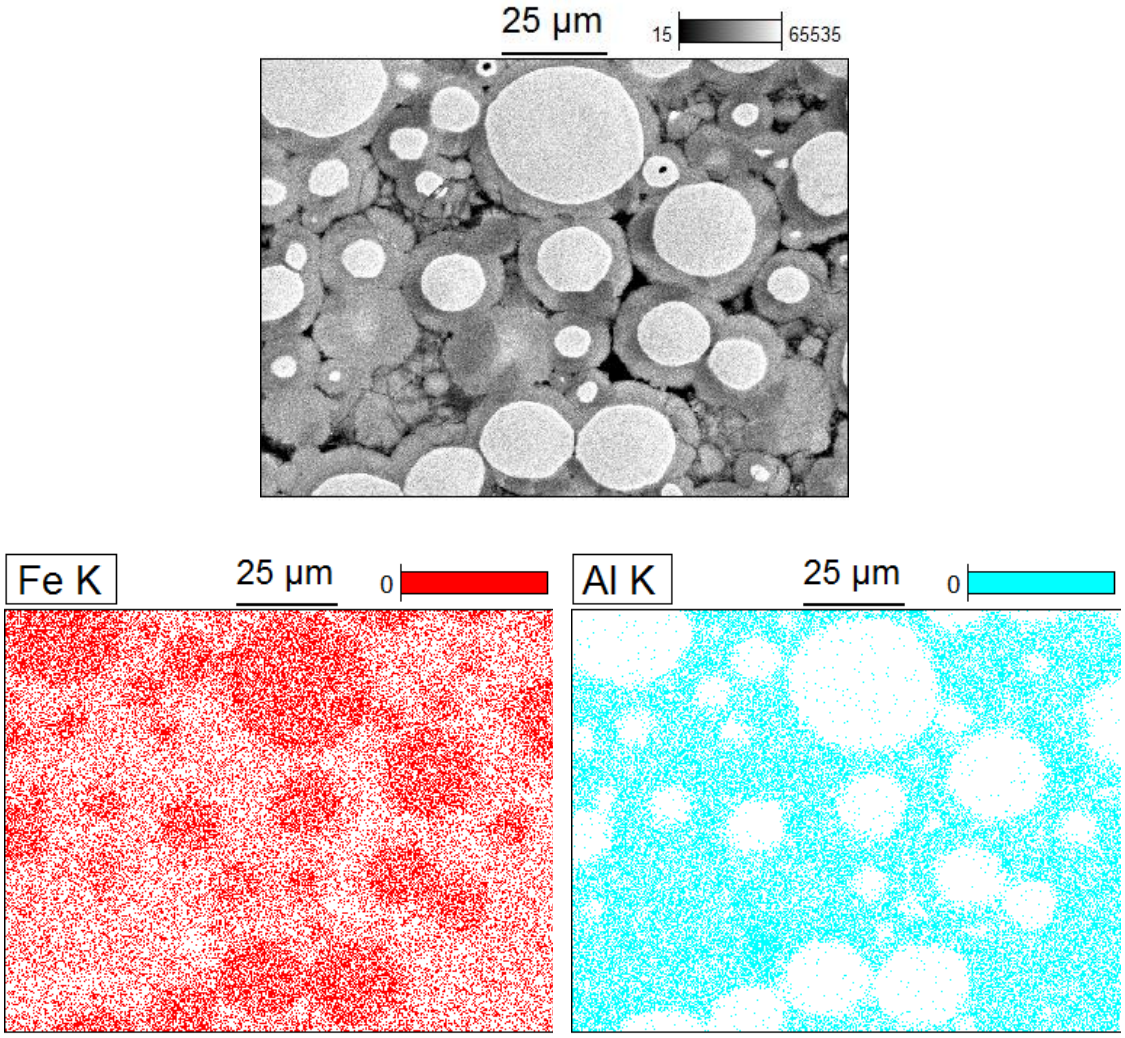

Figure 10. Fe and Al maps from a selected area of the cross-section of the composite obtained by SPS of the Al–50 vol.% $Fe_{66}Cr_{10}Nb_5B_{19}$ powder mixture at 570 ºC.

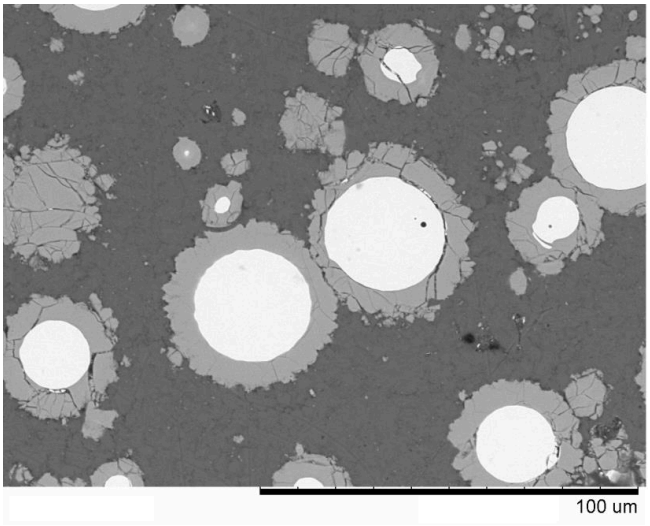

Figure 11. Cross-section of the composite obtained by SPS of the Al–20 vol.% $Fe_{66}Cr_{10}Nb_5B_{19}$ powder mixture at 500 ºC followed by annealing at 570 ºC.

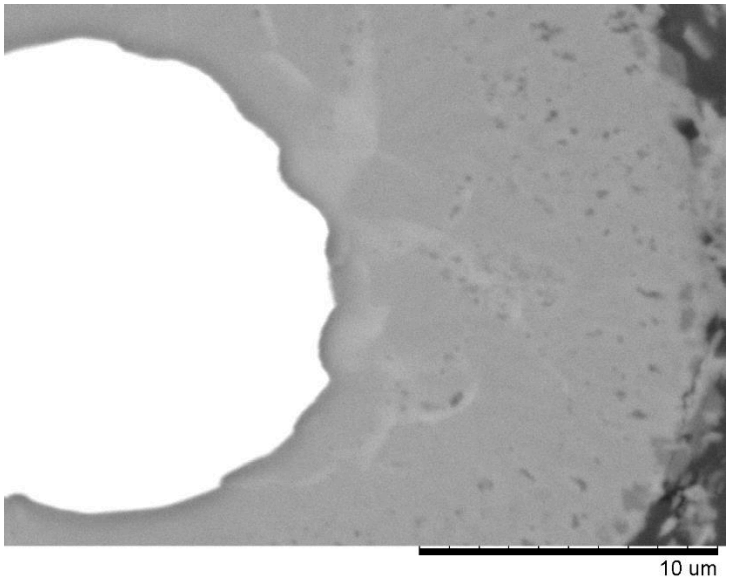

a

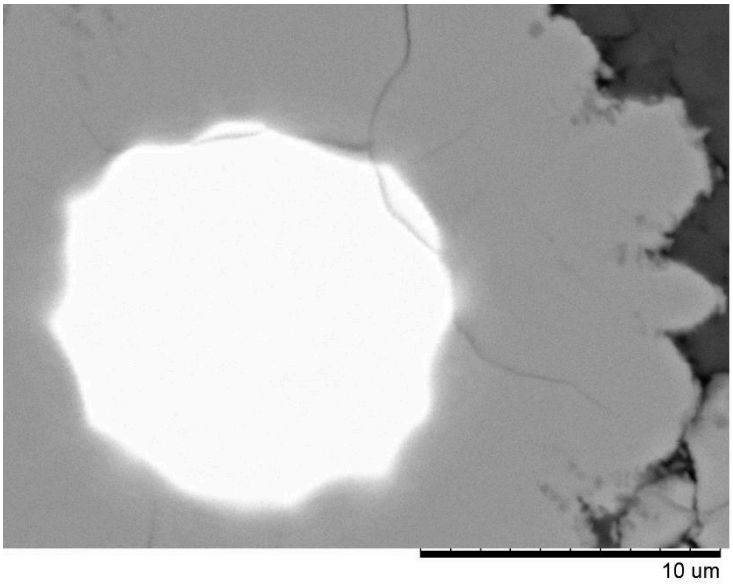

b

Figure 12. Reaction layer forming at the interface in composites obtained from the Al–20 vol.% $Fe_{66}Cr_{10}Nb_5B_{19}$ powder mixture: (a) SPS at 570 ºC and (b) SPS at 500 ºC followed by annealing at 570 ºC.

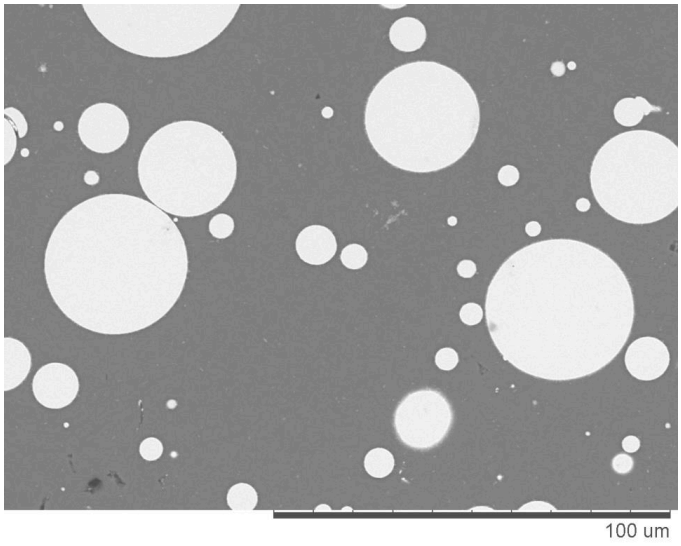

Figure 13. Cross-section of the composite obtained by SPS of the pre-compacted Al–20 vol.% $Fe_{66}Cr_{10}Nb_5B_{19}$ pellet, SPS at 540 ºC.

Table 1. Vickers hardness of the Al–$Fe_{66}Cr_{10}Nb_5B_{19}$ composites and microhardness of individual phases/characteristic regions, SPS at 540 ºC.

Al/ $Fe_{66}Cr_{10}Nb_5B_{19}$ volume ratio	Rela-tive density, %	Micro-hardness of Al matrix, $HV_{0.01}$	Micro-hardness of Fe-based cores, $HV_{0.01}$	Hardness of the composite, $HV_{0.3}$	Hardness – Reuss model*, HV	Hardness – Voigt model*, HV
80/20	97	44±1	1570±120	75±14	55	349
80/20, cold-pressed	97	47±7	1520±110	62±8	58	342

* calculated for the two-phase Al–20 vol.% $Fe_{66}Cr_{10}Nb_5B_{19}$ composite

Table 2. Vickers hardness of the Al–$Fe_{66}Cr_{10}Nb_5B_{19}$ composites and microhardness of individual phases/characteristic regions, SPS at 570 ºC.

Al/ $Fe_{66}Cr_{10}Nb_5B_{19}$ volume ratio*	Poro-sity**, %	Micro-hardness of Al matrix, $HV_{0.01}$	Micro-hardness of reaction layer, $HV_{0.01}$	Micro-hardness of Fe-based cores, $HV_{0.01}$	Hardness of the composite, HV_1	Hardness – Reuss model, HV	Hardness – Voigt model, HV
80/20	<1	63±7	860±70	1440±90	280±40	152***	612***
50/50	~6	-	930±50	1420±70	440±40	-	-

* Al/ $Fe_{66}Cr_{10}Nb_5B_{19}$ volume ratio is given for the powder mixture before sintering.

**determined from the analysis of the cross-sectional SEM images

*** calculated using volume fraction of the phases determined from the image analysis in ImageJ software